

A Modified Multivariate Madden–Julian Oscillation Index Using Velocity Potential

MICHAEL J. VENTRICE

*Department of Atmospheric and Environmental Science, University at Albany, State University of New York,
Albany, New York*

MATTHEW C. WHEELER AND HARRY H. HENDON

Centre for Australian Weather and Climate Research, Bureau of Meteorology, Melbourne, Australia

CARL J. SCHRECK III

*Cooperative Institute for Climate and Satellites, North Carolina State University, and NOAA/National Climatic
Data Center, Asheville, North Carolina*

CHRIS D. THORNCROFT

*Department of Atmospheric and Environmental Science, University at Albany, State University of New York,
Albany, New York*

GEORGE N. KILADIS

Physical Sciences Division, NOAA/Earth System Research Laboratory, Boulder, Colorado

(Manuscript received 7 November 2012, in final form 7 July 2013)

ABSTRACT

A new Madden–Julian oscillation (MJO) index is developed from a combined empirical orthogonal function (EOF) analysis of meridionally averaged 200-hPa velocity potential (VP200), 200-hPa zonal wind (U200), and 850-hPa zonal wind (U850). Like the Wheeler–Hendon Real-time Multivariate MJO (RMM) index, which was developed in the same way except using outgoing longwave radiation (OLR) data instead of VP200, daily data are projected onto the leading pair of EOFs to produce the two-component index. This new index is called the velocity potential MJO (VPM) indices and its properties are quantitatively compared to RMM. Compared to the RMM index, the VPM index detects larger-amplitude MJO-associated signals during boreal summer. This includes a slightly stronger and more coherent modulation of Atlantic tropical cyclones. This result is attributed to the fact that velocity potential preferentially emphasizes the planetary-scale aspects of the divergent circulation, thereby spreading the convectively driven component of the MJO's signal across the entire globe. VP200 thus deemphasizes the convective signal of the MJO over the Indian Ocean warm pool, where the OLR variability associated with the MJO is concentrated, and enhances the signal over the relatively drier longitudes of the equatorial Pacific and Atlantic. This work provides a useful framework for systematic analysis of the strengths and weaknesses of different MJO indices.

1. Introduction

The Madden–Julian oscillation (MJO; Madden and Julian 1971, 1972) is the most dominant mode of intraseasonal variability across the tropics. It is a

planetary-scale, baroclinic disturbance in circulation that is coupled to large-scale variations in convection. The MJO convective signal propagates eastward along the equator at about 5 m s^{-1} , and is primarily confined to the Eastern Hemisphere, although its circulation signal influences the global tropics (Hendon and Salby 1994). Not all MJO events traverse the globe, with the local periodicity of about 50 days presumably arising from the time scale set by the interaction between convection and dynamics that is fundamental to the MJO (e.g., Zhang 2005).

Corresponding author address: Michael Ventrice, University at Albany, State University of New York, 1400 Washington Ave., Albany, NY 12222.
E-mail: mventrice@albany.edu

The MJO not only influences the weather and climate throughout the global tropics but it also drives global teleconnections. The local impacts and remote teleconnections of the MJO are of wide interest because the long time scale of the MJO suggests the potential to make extended range predictions. Because of the primary role that monsoons play in the global climate and world economy, much focus has been dedicated to understanding the MJO's influence on the monsoons of North and South America, Africa, India, Asia, and Australia (e.g., Hendon and Liebmann 1990; Sperber et al. 2000; Higgins and Shi 2001; Jones and Carvalho 2002; Goswami et al. 2003; Carvalho et al. 2004; Annamalai and Sperber 2005; Matthews 2004; Wheeler and Hendon 2004, hereafter WH04; Wheeler and McBride 2005; Waliser 2006; Lavender and Matthews 2009). Of particular interest for the present study, the MJO's role in modulating tropical cyclone activity has been examined across all ocean basins (e.g., Nakazawa 1986; Liebmann et al. 1994; Maloney and Hartmann 2000a,b; Mo 2000; Higgins and Shi 2001; Hall et al. 2001; Bessafi and Wheeler 2006; Frank and Roundy 2006; Barrett and Leslie 2009; Maloney and Shaman 2008; Belanger et al. 2010; Kim et al. 2008; Klotzbach 2010; Schreck and Molinari 2011; Ventrice et al. 2011). The MJO has also been linked to the timing and intensity of the El Niño–Southern Oscillation (ENSO; McPhaden 1999; Takayabu et al. 1999; Zhang and Gottschalck 2002; Bergman et al. 2001; Lau 2005). A key step in the diagnosis of these impacts and teleconnections, especially from the perspective of monitoring and prediction of the associated climate/weather impacts, is the precise identification of the state (i.e., phase and amplitude) of the MJO.

WH04's multivariate principle component (PC) analysis is currently the most commonly used method to describe the state of the MJO. Their index, which they refer to as the Real-time Multivariate MJO (RMM) index, consists of the leading pair of PCs from a combined empirical orthogonal function (EOF) analysis of meridionally averaged (15°N – 15°S) outgoing longwave radiation (OLR), 200-hPa zonal wind (U200), and 850-hPa zonal wind (U850). The fundamental success of the RMM index for diagnosing the MJO in real time and in forecasts stems from the simplicity of the approach, which effectively leads to the discrimination of the MJO without the need for bandpass time filtering. This temporal discrimination results from the spatial projection onto equatorially averaged fields and the use of combined measures of convection (OLR) and circulation (zonal wind). By projecting onto the equatorially averaged, three-component eigenvector, higher-frequency variability is damped because it typically has smaller spatial scales or lacks the coherent variation between

convection and zonal wind that is the hallmark of the MJO (WH04). The use of OLR and zonal winds in the upper and lower troposphere also effectively discriminates the first baroclinic structure of the MJO, thereby eliminating other phenomena that are not as coupled in the vertical.

The availability of this index in real time has facilitated the monitoring and prediction of the MJO and its various impacts but some limitations have been noted. One limitation stems from the use of just two EOFs to define the MJO, which necessarily just depict its canonical large-scale structure. The tacit assumption in the approach of WH04 is that the MJO has a consistent broadscale expression in circulation and convection, which will be efficiently detected by the RMM indices. However, not every MJO event evolves with the same structure, even at the largest scales (e.g., Goulet and Duvel 2000), so the use of a single pair of EOFs cannot capture all the nuances of every MJO event, especially at smaller scales where the MJO expresses itself on local weather. Development of the RMM indices without the use of a bandpass filter also means that there will be some contamination from higher-frequency "noise" (e.g., Roundy et al. 2009).

The RMM indices from WH04 may also not be optimal for detecting the initiation of some MJO events when a large-scale circulation signal is absent (e.g., Straub 2013). It has also been suggested that by using equatorially averaged OLR as input, the RMM indices may have limited capability of detecting the MJO when its convective signal shifts into one hemisphere (Ventrice et al. 2011). Convective variations associated with the MJO are often asymmetric about the equator during the solstitial seasons.

This study, which explores the benefits of an alternative MJO index, began when the first author noted an improvement in some aspects of the RMM index when the OLR component of the index is replaced by 200-hPa velocity potential (VP200). In particular, differences were found in the representation of the MJO and its impacts over the Western Hemisphere. Documenting and understanding these differences is the aim of this paper.

Velocity potential is the inverse Laplacian of the divergence (e.g., Haltiner and Williams 1980). The inverse Laplacian acts as an effective spatial-smoothing operator, so VP200 essentially describes the gravest planetary-scale characteristics of the upper-level divergence (e.g., Hendon 1986). OLR, in contrast, identifies the more regional characteristics of the divergence. On the downside, the planetary scale of the VP200 might limit the ability to track precise details of the spatial distribution of convection and may give the perception of continuous

global propagation of a divergent component of the MJO (e.g., Lorenc 1984; Xue et al. 2002), when in fact the convective signal is primarily confined to the Eastern Hemisphere (Hendon and Salby 1994). However, VP200 naturally discriminates to the planetary scales of divergence that are more directly associated with the MJO, and likely enhances the capability to detect both symmetric and asymmetric components of convection about the equator. We delve further into the nuances of using VP200 instead of OLR to define a new MJO index in this paper.

Section 2 discusses the datasets and methodology of deriving the new index. Section 3 evaluates the strengths and weakness of this new index, especially for monitoring and detecting local impacts of the MJO on convective variability and tropical cyclones in the Atlantic sector. Conclusions are given in section 4.

2. Datasets and methodology

a. Datasets

The construction of the new MJO index is similar to WH04, using upper- and lower-tropospheric zonal winds (U200 and U850), but here we use VP200 rather than OLR to depict the convective/divergence variations. We obtain U200, U850, and compute VP200, from the Interim European Centre for Medium-Range Weather Forecasts (ECMWF) Re-Analysis (ERA-Interim) dataset (Dee et al. 2011). This analysis is available with 1.5° horizontal resolution and is used for the period 1990–2009. The temporal resolution of the data is 6-hourly, but we create daily averages prior to the EOF calculation. For comparison to WH04 and for diagnosing convective variations, we use daily gridded OLR obtained from the National Oceanic and Atmospheric Administration (e.g., Liebmann and Smith 1996). These daily data are available on a 2.5° grid and cover the same period as the ERA-Interim.

b. EOF analysis

Similar to the methodology of WH04, the input fields of U200, U850, and VP200 are equatorially averaged (15°N–15°S) and the time mean and first four harmonics of the climatological seasonal cycle are removed. Low-frequency (interannual) variations are removed by subtracting a 120-day running average. So that these EOFs can be applicable in real time, the running average is based on the previous 120 days (i.e., it is not centered; Gottschalck et al. 2010). Unlike WH04, the linear variability associated with the ENSO is not subtracted from the raw fields. This step was deemed to be unnecessary, as the removal of the 120-day mean has been found to be

sufficient (Lin et al. 2008). Prior to the EOF calculation, the individual anomaly fields were normalized by the square root of the longitudinally averaged variance of the respective fields prior to concatenating into a combined three-component input field that we denote as $X_j(i, t)$, where $j = 1-3$, i refers to longitudinal points along the equator, and t is time.

For the remainder of this paper, we denote the leading pair of PCs of the EOFs calculated from U200, U850, and VP200 as the velocity potential MJO (VPM) indices. We compare them to the PCs and EOFs computed by WH04, which we refer to as the RMM indices. The RMM indices, which are based on U850 and U200 from the National Centers for Environmental Prediction–National Center for Atmospheric Research (NCEP–NCAR) reanalysis (Kalnay et al. 1996) and satellite OLR (Liebmann and Smith 1996) are obtained online (<http://www.cawcr.gov.au/staff/mwheeler/maproom/RMM/>). For the RMM PCs, the EOF analysis was performed using data for 1979–2001, and subsequent PC values have been computed by projecting the daily data onto the fixed EOF spatial patterns.

c. EOF-based reconstruction

For the analysis in section 3, we will make use of fields that are reconstructed from the two-component indices. The reconstruction can be done in two fashions. First, the EOFs and PCs can be used directly to reconstruct the input fields. The three-component reconstructed fields are given as

$$\hat{X}_j(i, t) = \text{EOF}_{1j}(i) \times \text{PC}_1(t) + \text{EOF}_{2j}(i) \times \text{PC}_2(t), \quad (1)$$

where $\hat{X}_j(i, t)$ is the j th component of the reconstructed anomaly field and EOF_{1j} and EOF_{2j} are the j th components of the three-component eigenvector. Since the three input fields were normalized (by the square root of the longitudinally averaged variance) before the EOF analysis, this will provide normalized output that can be converted to unnormalized values by multiplying by the normalization factors.

This direct reconstruction using the PCs and eigenvectors is limited to the input fields. Reconstruction can also be based on multiple linear regression. In this case, it can be performed for any field, and it is not limited to the longitudinal dimension along the equator. That is, we can reconstruct fields in two spatial dimensions as well as in time. A typical reconstruction of a two-dimensional spatial field $Y(i, k, t)$ using the pair of PCs as predictors is given by

$$Y(i, k, t) = A_1(i, k) \times \text{PC}_1(t) + A_2(i, k) \times \text{PC}_2(t), \quad (2)$$

where k represents latitude and A1 and A2 are developed using least squares multiple regression of the independent field Y onto the dependent predictors (PC1 and PC2). Note that the regression can be done separately for each season in order to capture seasonal variations of the local relationship of the field with the MJO, or the regression can be done across the entire data record to capture seasonally independent behavior.

The explained variance of the total input field $X_j(i, t)$ by each EOF is given by the eigenvalue, or, equivalently, by the mean spatial variance of the eigenvector across all three components. Similarly, the explained variance of the subcomponent of the input field is the mean spatial variance of the associated subcomponent of the eigenvector. The explained variance of the subcomponents of the input field will be of interest for comparison between the VPM EOFs that use VP200 and the original RMM EOFs that use OLR. We will demonstrate that the explained variance of the input VP200 fields will be higher for the VPM EOFs compared to the explained variance of the input OLR field for the original RMM indices because VP200 is a smoother, more planetary-scale field. This higher loading from the convective/divergent component for the VPM EOFs provides additional sensitivity to the VPM indices for detecting MJO events where the OLR component is weak near the equator (especially during boreal summer).

3. The new velocity potential MJO index

a. Results of the EOF analysis

The spatial structures (eigenvector) of the leading three EOFs of the combined fields of U200, U850, and VP200 are shown in Fig. 1. The explained variances (eigenvalues) of EOF1 (22%) and EOF2 (20%) are similar and suggestive of a pair. Taking the first two EOFs as a pair, their summed explained variance is 42.5%, while EOF3 explains only 6.8% of the variance. Therefore, the first two EOFs are well separated from the third according to the criteria of North et al. (1982). The summed variance of EOF1 and EOF2 from the RMM EOFs (i.e., from WH04) explain only 25% of the variance. The higher explained variance here for the VPM EOFs is attributed to the use of VP200, which is much less spatially and temporally noisy than OLR.

While each input field of the combined EOF analysis should have exactly the same input variance due to the normalization that was applied, each EOF will not have an equal contribution from each field to its variance. For example, in the RMM EOFs of WH04, OLR contributes less variance to EOF1 and EOF2 than the zonal wind fields, but to make up for that it must contribute more

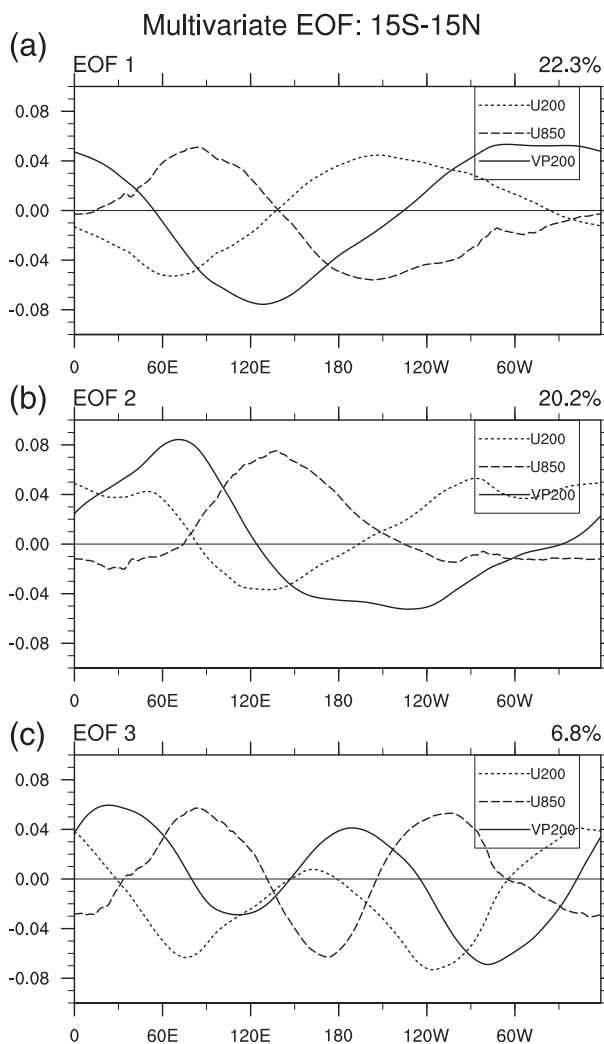


FIG. 1. Spatial structures of EOFs 1, 2, and 3 of the combined analysis of anomalous U200, U850, and VP200. EOFs are constructed by using data averaged over 15°S–15°N, including all longitudes. Magnitudes are plotted on the same relative axis. The variance explained by the respective EOFs is 22.3%, 20.2%, and 6.8%, respectively.

than the winds in some higher-order EOFs. One method to compute the fractional contribution of each variable to the leading pair of EOFs is to first compute the fraction that each variable contributes to PC1 and PC2 on each day. This is given by

$$\text{Fraction}_x(t) = \frac{\text{PC1}_x(t) \times \text{PC1}(t) + \text{PC2}_x(t) \times \text{PC2}(t)}{\text{PC1}(t)^2 + \text{PC2}(t)^2}, \quad (3)$$

where Fraction_x represents the fractional contribution of a particular variable x at a particular time t , PC_x is the projection of a particular variable onto its portion of the

EOF, PC1 and PC2 are the full PCs computed using the contribution of all three variables, and $PC1(t)^2 + PC2(t)^2$ is the square of the amplitude of the normalized PCs. These fractional contributions can then be averaged over all times to compute the average contribution of each variable to the leading pair of EOFs. For WH04's RMM indices, the fractional contribution of the total explained variance of the first two EOFs for OLR is 14.7%, which compares to 43.9% for U850 and 41.4% for U200. For the VPM indices, the explained variance for U850 and U200 is 25.4% and 26.5%, respectively, and for VP200 it is 48.1%. Therefore, the relative loading on the convective/divergence part of the VPM EOFs is higher than for the RMM EOFs, suggesting that the VPM EOFs will be more sensitive to large-scale divergence.

The spatial structure and phasing of the individual fields for the leading two VPM EOFs is similar to that for the RMM EOFs (i.e., Fig. 1 in WH04) but there are some subtle differences. VPM EOF1 (Fig. 1a) represents times when upper-level divergence occurs at the longitude of the Maritime Continent (90°–135°E) with lower-tropospheric westerlies underlying upper-tropospheric easterlies farther to the west over the Indian Ocean. Upper-level convergence and lower-tropospheric easterlies/upper-tropospheric westerlies are centered over the eastern Pacific, with upper-level convergence farther to the east over the Atlantic sector. VPM EOF2 (Fig. 1b) appears to capture the MJO at about 1/4 cycle later, with upper-level divergence now shifted to over the central-east Pacific and lower-tropospheric westerlies over the Maritime Continent. Upper-level convergence is seen over Africa and the Indian Ocean (15°W–120°E). For reference we also show VPM EOF3 (Fig. 1c), which is dominated by a wavenumber-2 structure in all three variables unlike what is usually associated with the MJO; hence, we ignore EOF3 and all higher EOFs for the rest of the discussion.

Comparing the VPM EOFs to WH04 (their Fig. 1), the spatial structure of the U850 and U200 components for both EOF1 and EOF2 are nearly identical. However, the loading on VP200 in the VPM EOFs clearly has more weight in the Western Hemisphere than does the loading on OLR as used in WH04. That is, the OLR signal in the RMM indices is largely confined to the Eastern Hemisphere, whereas the convergence/divergence signal in the VPM EOFs as depicted by VP200 appears to have more equal variance across the tropics. The benefit and cost of this enhanced sensitivity to convective/divergence variations by using VP200 will be further discussed below.

To demonstrate that the new indices effectively discriminate the time scales of the MJO, power spectra of

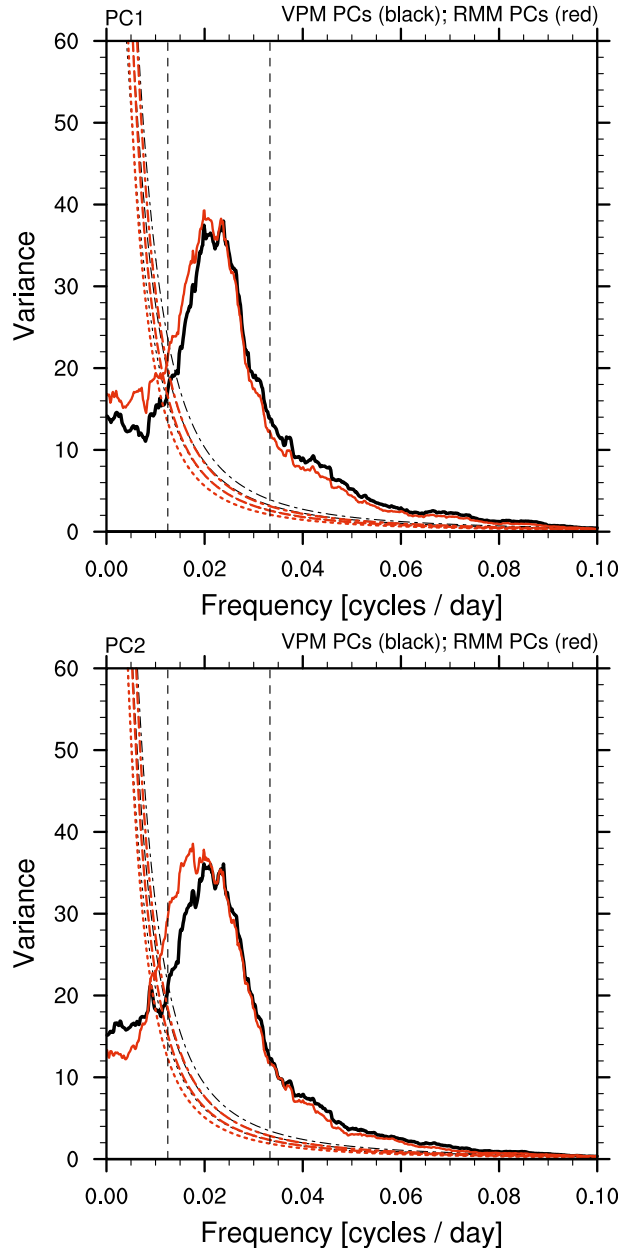


FIG. 2. Power spectra of the PCs for the leading two EOFs of combined fields shown of Fig. 1. The original EOFs from WH04 are also included and indicated by the red line. The curved-dashed black and red lines represent the red-noise spectrum for the VPM PCs and RMM PCs, respectively. The upper limit represents the 95% confidence interval and the lower limit represents the 5% confidence interval. The two vertical dashed lines represent the 30–80-day range.

the VPM PCs (black lines) are shown in Fig. 2. We also include the spectra of the original RMM indices (red lines) for comparison. As for the original RMM indices, the VPM PCs exhibit a pronounced spectral peak in the MJO range (30–80-day period). VPM PC2 contains

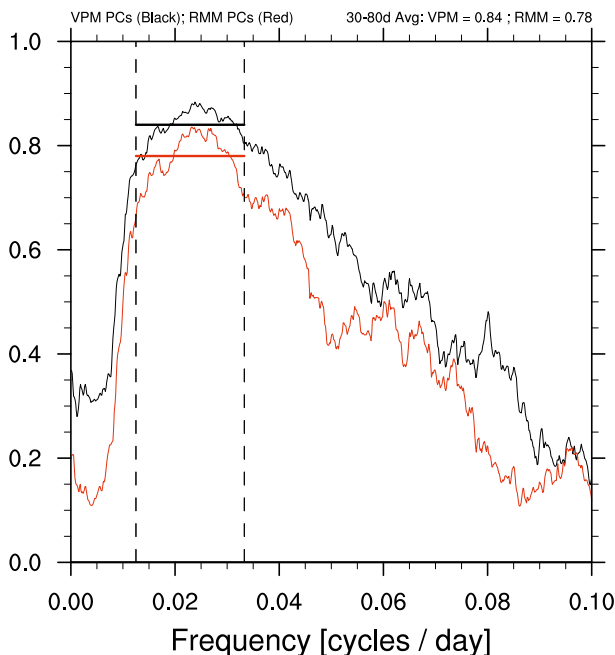


FIG. 3. Coherence squared between PC1 and PC2 of the VPM EOF analysis of Fig. 1 (black line) and between PC1 and PC2 of an EOF analysis using the atmospheric fields associated with the RMM EOFs (OLR, U200, U850; red line). Smoothing was applied to the cospectrum before computing the phase and coherence. The vertical dashed lines represent the 30–80-day range.

slightly less power at the lower-frequency end of the intraseasonal range compared to RMM. Overall, however, the VPM PCs appear to discriminate the time scales of the MJO equally well as the RMM PCs.

The cross-power spectrum of the PCs is another way to verify that the leading EOFs are a pair that describes the eastward-propagating characteristics of the MJO. Figure 3 shows the coherence squared (Coh^2) of the leading pair of VPM PCs and that of the original RMM PCs for comparison. The Coh^2 between the new PCs peaks in the 30–80-day range, with a mean value of 0.84 and a phase lag of $1/4$ cycle (i.e., PC1 leads PC2 by 15 days, not shown), confirming that the leading pair of the VPM EOFs is depicting coherent eastward propagation. The corresponding Coh^2 for the original RMM indices is 0.78, also with a phase lag of $1/4$ cycle. Hence, both the new and old leading pair of EOFs describe a similar eastward propagation of the MJO, although with slightly more coherence in the VPM PCs.

b. Reconstructed fields

As a further check on the adequacy of the new index for capturing the structure and behavior of the MJO, reconstructed fields are examined to see the degree to

which the signal of the MJO is represented by the pair of PCs. Here we concentrate on the reconstruction of the convective variability captured by the index as we anticipate that this is the field that will show the most difference between the VPM and RMM EOFs. In Fig. 4, we show the space–time spectra of the observed OLR (i.e., the OLR anomaly averaged 15°N – 15°S) and the reconstructed OLR as given by the regression technique in Eq. (2) using the new PCs. To emphasize that the VPM EOFs are cleanly extracting the signal of the MJO and are not being contaminated by other disturbances with similar spatial structure but at higher frequency (e.g., Roundy et al. 2009), we also display in Fig. 4 the ratio between the power spectra of the reconstructed and input OLR fields, along with the ratio based on the original RMM. The capability of the new PCs to discriminate the MJO spectral peak at eastward-propagating zonal wavenumbers 1–3, and periods between 30 and 80 days is clearly illustrated in the reconstructed OLR field, for which the reconstruction from the VPM EOFs explains approximately 65% of the spectral peak at wavenumber 1 in the original OLR dataset, compared to about 56% for the RMM EOFs. Consistent with the spatially smoothed nature of VP, the reconstruction using the VPM EOFs captures slightly more of the wavenumber-1 spectral peak in OLR than does the reconstruction using the RMM EOFs, although the RMM EOFs capture more of the MJO’s OLR signature at wavenumbers 2 and 3. Importantly, both approaches can be seen to be adept at removing contributions from higher-frequency convectively coupled atmospheric Kelvin waves and westward-propagating Rossby waves (see WH04 for further explanation).

We have also computed the space–time power spectrum of U850 reconstructed from the VPM and RMM PCs (not shown). For both the VPM and RMM PCs, the reconstructed fields capture upward of 90% of the spectral peak at eastward zonal wavenumber 1 and periods 30–80 days. Hence, we conclude that the VPM EOFs are capable of identifying the prominent large-scale structure of the MJO.

The potential benefit of identifying the MJO through use of VP200 instead of OLR is further demonstrated in Fig. 5, which shows an example of reconstructed OLR (left) and VP200 (right) using the VPM EOFs for the period from June 1996 to June 1997. Coherent eastward-propagating anomalies associated with the MJO are depicted in both the OLR and VP200, emphasizing the capability of the new PCs to discriminate the periodicity and spatial structure of the MJO without the need for bandpass time filtering (see also WH04). The VP200 anomalies are seen to be collocated with the same signed OLR anomalies. Importantly, however, the VP200

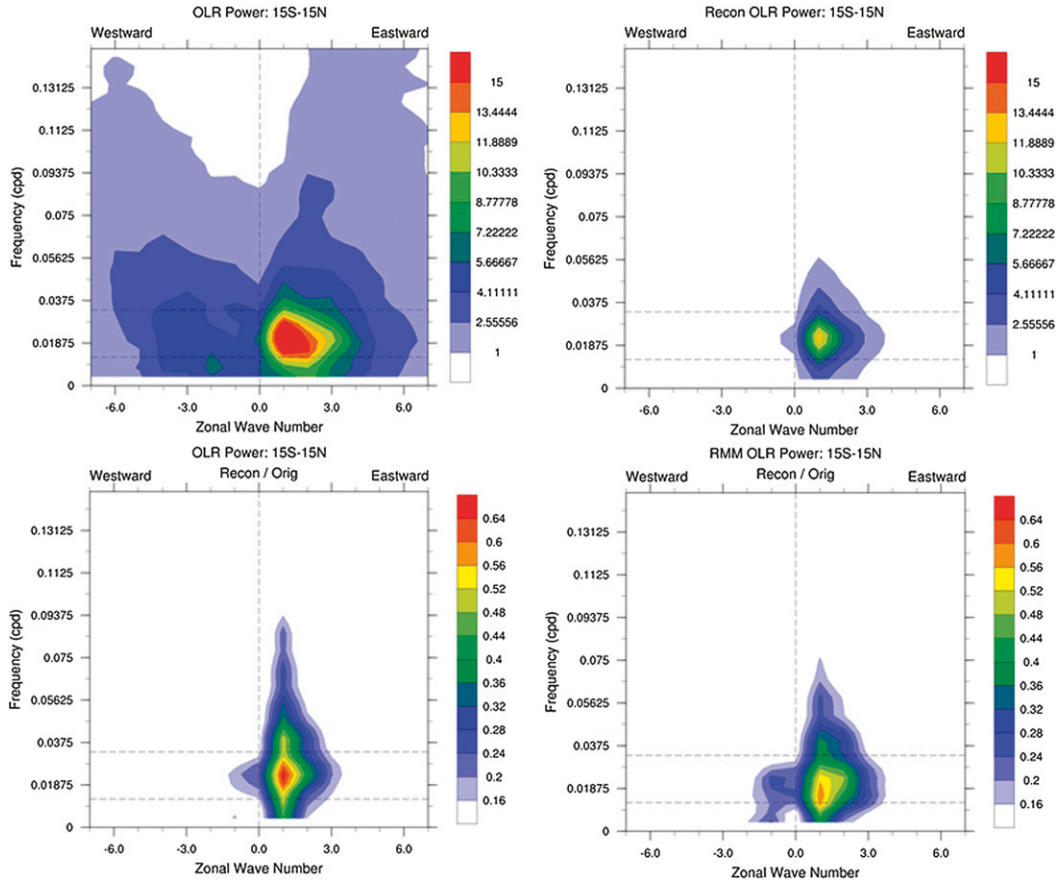


FIG. 4. Space–time power between (top left) 15°S–15°N averaged raw OLR and (top right) reconstructed OLR from the VPM EOFs, (bottom left) the ratio between the raw OLR and reconstructed OLR using the VPM EOFs, and (bottom right) the ratio between the raw OLR and reconstructed OLR using the RMM EOFs. The two horizontal dashed lines represent the 30–80-day range.

anomalies circumnavigate the globe while OLR anomalies are far less continuous and are confined to (mostly the Eastern Hemisphere) where convective variance is most concentrated. This cessation of the OLR anomaly at about the date line reflects the strong dependence of convection on sea surface temperature. However, the reconstructed VP200 field appears to have no such constraint, and often the VP200 signal is present over the longitudes of Africa before the “initiation” of convection (as indicated by the OLR) over the Indian Ocean. It is also notable that the phase speed of the VP200 signal is generally much faster than that of OLR, typically between 15 and 25 m s⁻¹, especially over the Western Hemisphere. Since VP is a strongly smoothed representation of the planetary-scale divergence field (Hendon 1986), its propagation does not necessarily reflect a convective signal propagating at this speed but is likely affected by the far-field divergence, as well as the fast dry Kelvin mode that is excited by the MJO (e.g., Milliff and Madden 1996; Sobel and Kim 2012).

To compare the behavior of the VPM and RMM EOFs in identifying the MJO, Fig. 6 shows the total number of days when the index amplitude ≥ 1 (defined as an “MJO day”) for all MJOs phases during all months (top), only boreal winter months (middle), and only boreal summer months (bottom). While we define an MJO day as a date where the index is greater than 1 sigma, it should be noted that there are times when the index can temporarily be greater than 1 sigma when no coherent MJO signal is present. This often occurs during times where noise (i.e., extratropical waves, convectively coupled atmospheric Kelvin waves, or equatorial Rossby waves) unrelated to the MJO project onto the PCs. We have tested another definition of an MJO day as defined by Straub (2013), where the index is greater than one standard deviation for a period no less than seven days. The results for this analysis are relatively unchanged when compared to the standard MJO day definition using just an amplitude threshold, with the exception of the tropical cyclone statistics, as there were

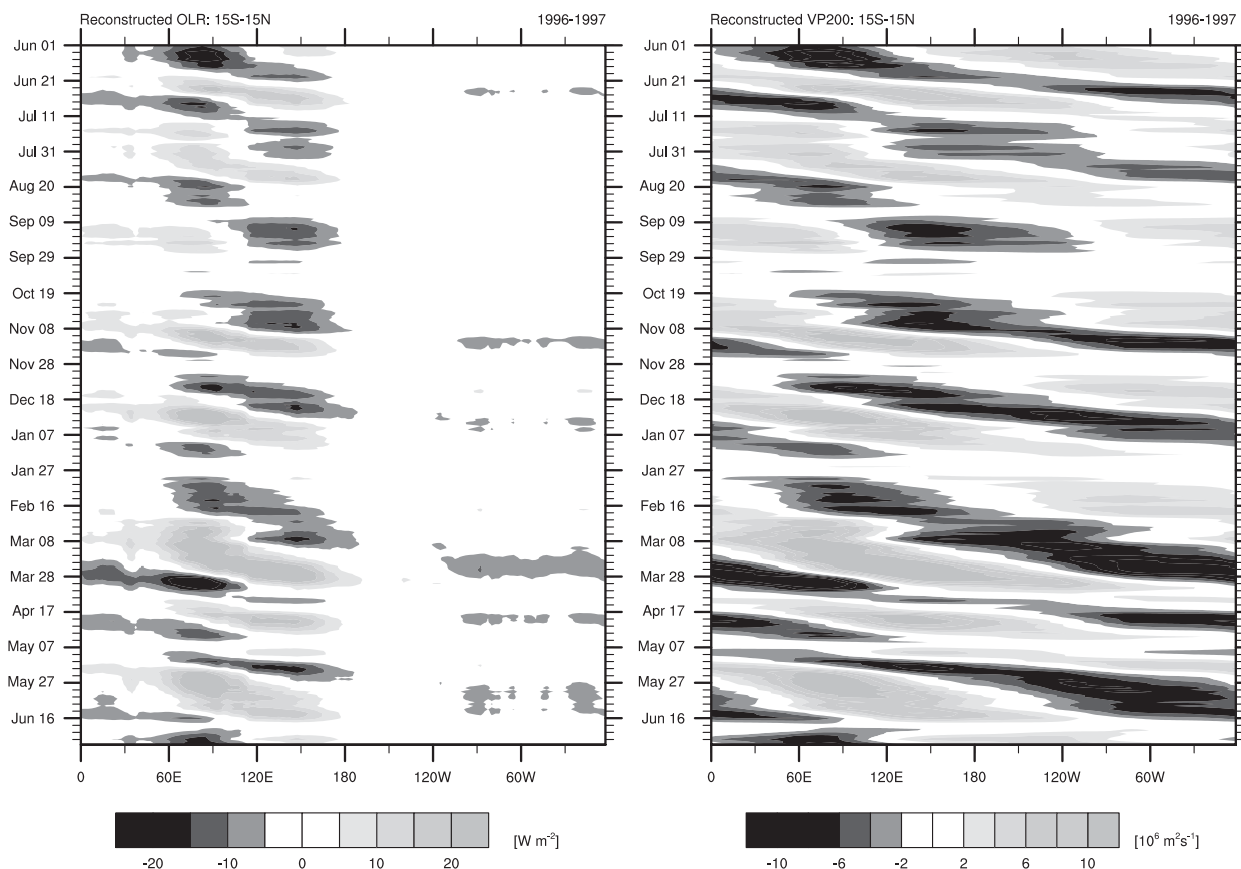


FIG. 5. Time-longitude plots of (left) reconstructed OLR and (right) reconstructed VP200 from the leading EOF pair of the VPM EOF analysis for the period between June 1996 and June 1997.

too few MJO days after applying the Straub (2013) methodology.

To begin, there are a total of 38 more MJO days using the VPM index rather than RMM in the 1990–2009 climatology. While the differences are subtle, the VPM captures a higher number of MJO days during phases 3, 5, 6, 7, and 8 when compared to RMM. This result is indicative of increased MJO identification by the VPM index, especially over the Pacific and Atlantic basins.

After dividing the number of MJO days for only boreal winter (November–February), the RMM captures a total of 61 more MJO days when compared to VPM. The increased number of boreal winter MJO days identified by RMM is during times when the MJO is located over the Maritime Continent and west Pacific (phases 4–7). This is a time when the South Pacific convergence zone becomes convectively active, thus indicating a benefit of using OLR over VP200. However, note that there are slightly more boreal winter MJO days over the Western Hemisphere and Indian Ocean (phases 8, 1, and 2) using VPM over RMM, suggesting that the VPM is capturing a slightly stronger Western Hemisphere MJO signal over RMM.

For boreal summer [June–September (JJAS)], an opposite relationship is found (with exception of the Western Hemisphere), where there are 85 more MJO days identified using VPM when compared to RMM. The VPM index captures more MJO days in all phases except when the MJO is present over the Indian Ocean (phases 1–2). This result suggests a potential use for the VPM index with regards to the summer monsoons, as well as tropical cyclone activity over the west and east Pacific, and the Atlantic basins. To investigate the differences between the two sets of indices during boreal summer, a composite analysis is shown below.

c. Boreal summer composites

Composite evolution of the MJO is developed following WH04 by defining eight distinct phases of the MJO. Each phase represents a time when the MJO is located over a different geographical location. Since the two VPM EOFs match the phasing of the RMM EOFs, the eight defined phases should nearly match those for the RMM. That is, phase 1 from the new index should best match phase 1 from the RMM index. We concentrate here on boreal summer (June–September) and

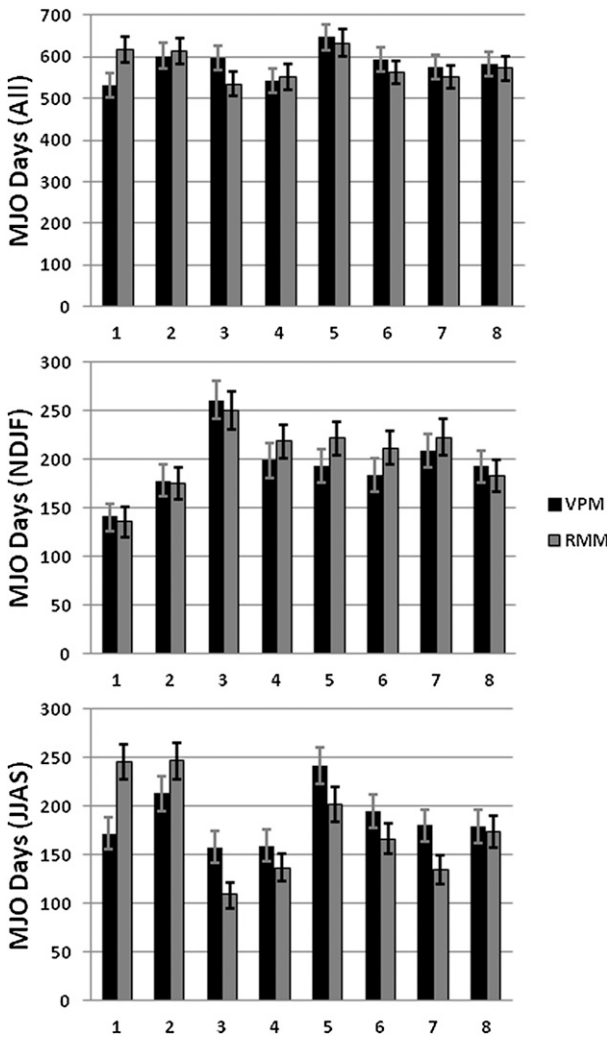


FIG. 6. The number of MJO days, defined as a day where the amplitude for the VPM (black) or RMM (gray) index was greater than or equal to one standard deviation, binned for all MJO phases during (top) all months; (middle) boreal winter (November–February) only months; and (bottom) boreal summer (June–September) only months. The 90% confidence interval is indicated by the error bars.

show composites based on the phases given by the VPM and RMM EOFs (Fig. 7). In these composites, anomalous VP200 is shaded and 200-hPa wind anomalies are shown as vectors. These composites are made by averaging over the set of days that the MJO was in a particular phase and when the amplitude of the index, defined as $(PC1^2 + PC2^2)^{1/2} \geq 1$ (noting that PC1 and PC2 are standardized by their long-term standard deviation).

According to Fig. 7, a clear MJO-wavenumber-1 signal is identified in VP200 for all MJO phases during boreal summer using both the RMM (Fig. 7a) and VPM (Fig. 7b) PCs. While the RMM index captures a similar

spatial MJO structure in VP200 (since it includes upper-tropospheric circulation information), it is weaker in magnitude when compared to the signal retained by the VPM PCs, especially during the MJO’s transit across the Western Hemisphere (phases 7–8) and when the MJO transitions from the Indian Ocean to over the Maritime Continent (phases 1–4). To further investigate whether the VPM PCs are more capable of identifying boreal summer MJO days, we consider more directly the role played by the MJO on convection. Figure 8 shows composites of OLR anomalies in June–September based on the MJO phases derived from the RMM (Fig. 8a) and VPM PCs (Fig. 8b). While the VPM PCs do not use OLR information, a similar MJO convective signature with respect to WH04’s RMM PCs is detected for all MJO phases. However, there are some noticeable differences between the two composites with regards to local convective anomalies over the Western Hemisphere, especially during MJO phase 3. Phase 3 is a time where RMM tends to struggle during boreal summer since it is a period consisting of an asymmetric MJO-convection signature over the Indian Ocean, where convection tends to be active over the Indian Continent, suppressed over the southwestern equatorial Indian Ocean, yet active over the eastern equatorial Indian Ocean. This gives an overall active MJO convection signature similar to a “boomerang” or backward “C.” Because of the latitudinal averaging technique of the combined EOF analysis, RMM will often weaken during boreal summer phase 3, especially when other disturbances (seasonal or subseasonal) influence convection patterns during this state. Note that there are also stronger negative OLR anomalies over Africa (as well as positive OLR anomalies over the equatorial east Pacific) during phase 3 when using the VPM PCs in comparison to the RMM PCs. A two-sided bootstrap resampling test was performed to compare both sets of OLR composites and the results showed that when using the VPM PCs, the positive OLR anomalies over the east Pacific and the negative OLR anomalies over Africa during phase 3 are statistically different than the anomalies using the RMM PCs at the 90% level (not shown). The enhanced OLR signal over Africa is suggestive that the VPM index may be capturing a better MJO–West African monsoon modulation. This enhanced African convection may be of important relevance to downstream Atlantic tropical cyclone modulation and genesis, which we further address below.

d. Modulation of Atlantic tropical cyclones

The MJO is of particular interest for medium-range predictability of tropical cyclogenesis. The MJO has been shown to modify tropical cyclogenesis over the

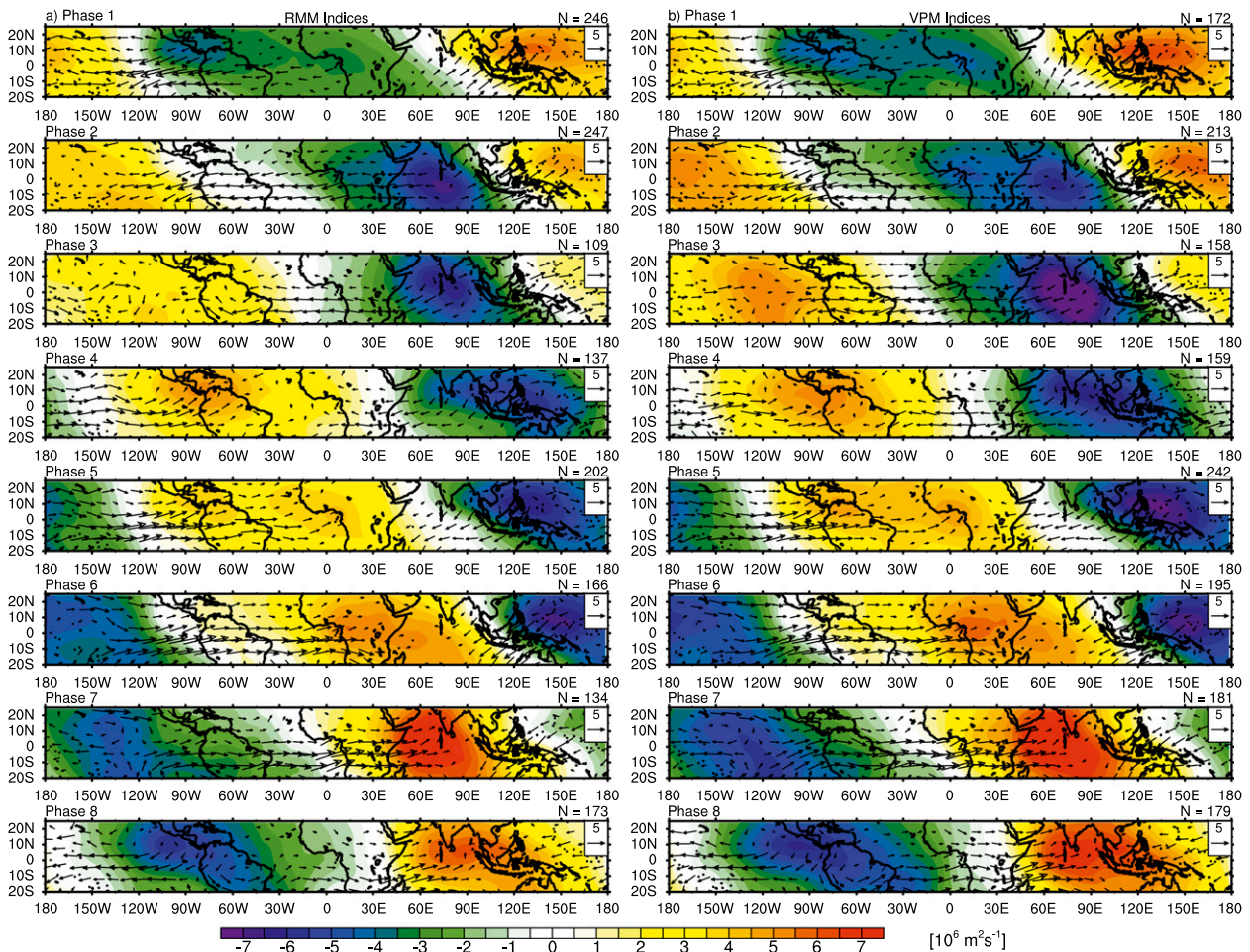


FIG. 7. JJAS composite of anomalous VP200 (shaded) and 200-hPa wind anomalies (vectors) for each phase using (a) the RMM PCs and (b) the VPM PCs. VP200 anomalies statistically different than zero at the 95% level are shaded. Negative VP200 anomalies represent upper-level divergence. The number of days in each phase N is provided. The reference vector is 5 m s^{-1} .

Atlantic (e.g., Maloney and Hartmann 2000a,b; Mo 2000; Higgins and Shi 2001; Barrett and Leslie 2009; Maloney and Shaman 2008; Belanger et al. 2010; Klotzbach 2010; Ventrice et al. 2011). Using the original RMM indices, Klotzbach (2010), Belanger et al. (2010), and Ventrice et al. (2011) all concluded that Atlantic tropical cyclogenesis was most likely during MJO phases 1–3, which is when enhanced convection associated with the MJO is located over the Indian Ocean. Using the VP200 MJO diagnostic derived by Xue et al. (2002), Barrett and Leslie (2009) found that tropical cyclones were most likely to occur in the Atlantic basin when negative VP200 anomalies were centered at about 80°E , which is roughly consistent with the phasing based on the WH04 index.

To investigate the possible enhanced utility of the VPM EOFs to detect the modulation of Atlantic tropical cyclones by the MJO, we count all tropical cyclones

that developed during June–September when the amplitude ≥ 1 and then we binned them by each phase of the MJO (Fig. 9a). We do this using both the VPM PCs and the original RMM indices. Tropical cyclogenesis is defined as the time when the National Hurricane Center classified a tropical cyclone as a tropical storm [sustained maximum winds of 34 kt ($\sim 17.5 \text{ m s}^{-1}$)].

In Fig. 9a, the number of Atlantic tropical cyclogenesis events is divided by the number of MJO days for both sets of PCs. This normalization is necessary since the total number of MJO days is different for each phase and each index. Atlantic tropical cyclogenesis is observed to occur in all eight MJO phases for both sets of PCs. However, the most favorable phase for genesis is phase 3 for both the VPM and RMM PCs (14.6% and 11.9%, respectively, of the total number of events). The least favorable MJO phase for genesis is phase 7 for both the VPM and RMM PCs (3.3% and 4.5%, respectively,

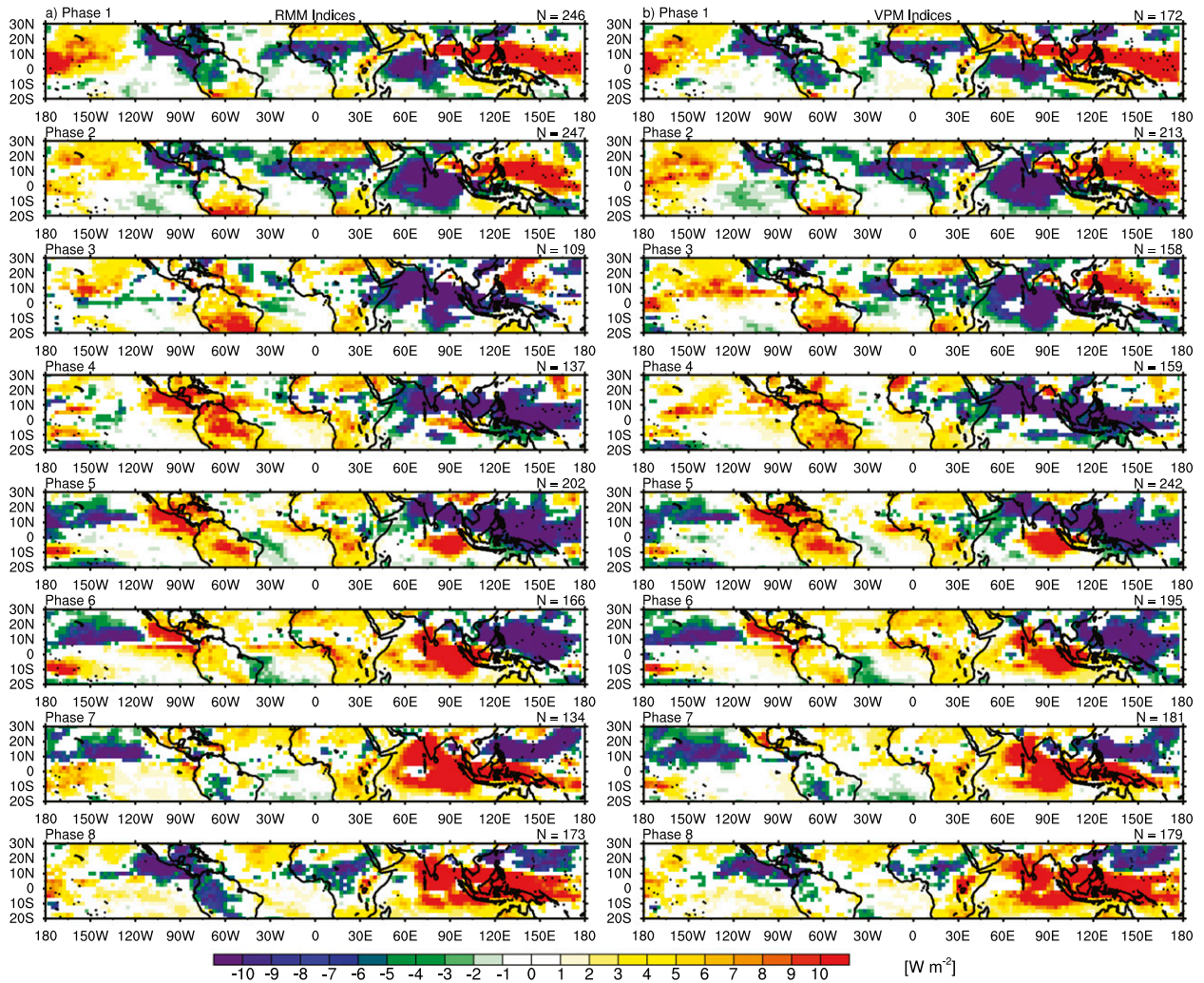


FIG. 8. JJAS composite of anomalous OLR (shaded) for each MJO phase using (a) the RMM PCs and (b) the VPM PCs using VP200 instead of OLR. Anomalies statistically different than zero at the 90% level are shaded.

of the total number of events). Using the VPM PCs, tropical cyclogenesis is about 4 times more likely during phase 3 than during phase 7. Using the RMM PCs, tropical cyclogenesis is less than 3 times as likely to develop during MJO phase 3 with respect to MJO phase 7. Hence, the VPM indexes appear to detect a slightly stronger modulation of Atlantic tropical cyclogenesis than does the RMM index.

The MJO modulates Atlantic tropical cyclones because it impacts the large-scale environment over the tropical Atlantic (e.g., Ventrice et al. 2011 and references therein). Therefore, we assume that the MJO might also affect the intensity of mature tropical cyclones there (e.g., Barrett and Leslie 2009; Klotzbach 2010). To investigate whether Atlantic hurricane activity varies coherently with the VPM PCs, hurricane days

(HDs) are binned for each MJO phase using the same MJO amplitude threshold as before (Fig. 9b). One HD is defined as a date when one or more tropical cyclones were active over the Atlantic and were associated with an intensity of greater than or equal to the Saffir–Simpson scale category-1 hurricane [64-kt ($\sim 33 \text{ m s}^{-1}$) maximum sustained winds]. Figure 9b shows the distribution of Atlantic hurricane days divided by the number of MJO days for each MJO phase for both of the VPM and RMM indices. The result shows that Atlantic hurricanes vary coherently with the MJO regardless of the MJO index that is used. Atlantic HDs are most favorable during phase 2 for both the VPM PCs and RMM PCs (26%). For the VPM PCs, there is a general reduction of normalized HDs after phase 2, with the minimum of HDs in phase 7 (4%). For the RMM PCs, the modulation

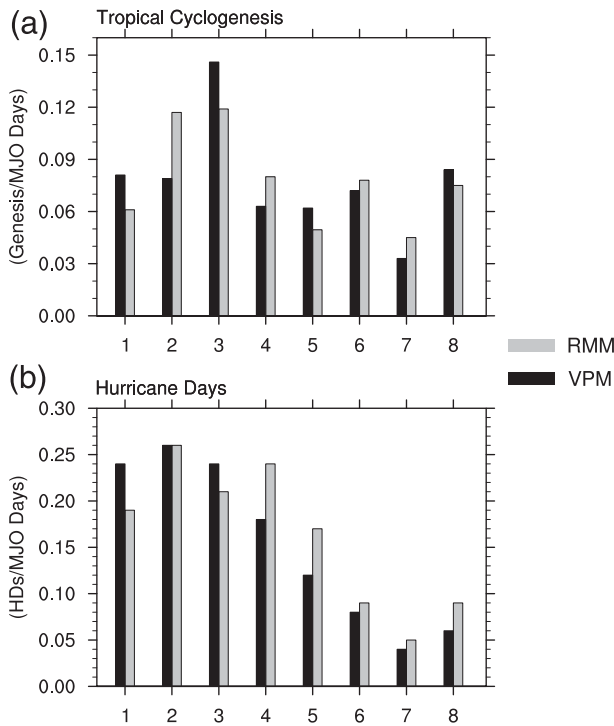


FIG. 9. (a) Normalized Atlantic genesis days and (b) normalized Atlantic hurricane days (HDs) for each MJO phase for the VPM PCs (black) and the RMM PCs (gray) during the JJAS (1989–2009) season. Both (a) and (b) are normalized by the number of MJO days for each particular MJO phase.

is more noisy, with a second peak of occurring during phase 4 (24%). Like the VPM PCs, a minimum of normalized HDs occur during phase 7 (5%) using the RMM PCs, but the overall modulation is not quite as strong. Hence, the VPM indices also show an enhanced capability to detect the modulation of HDs compared to the original RMM indices.

This relationship between the MJO and Atlantic hurricanes is consistent with the results of Barrett and Leslie (2009), who found that intense hurricanes are statistically significantly favored in the Atlantic's main development region when negative (positive) VP200 anomalies associated with the MJO are located over 80°E (120°W). This location of the MJO is most comparable to MJO phases 2 and 3 when using the VPM PCs (see Fig. 7).

In summary, the relationship between Atlantic tropical cyclogenesis and the MJO, as well as Atlantic hurricane frequency and the MJO, is slightly more robust when using the VPM index (comprising U200, U850, and VP200) compared to the original RMM index (comprising U200, U850, and OLR). This result is attributed to the VPM PCs being more sensitive to the modulation of divergence over the Atlantic sector because of the use of VP200 instead of OLR.

4. Conclusions

There is proven utility in having an index of the MJO that depicts its magnitude and location and that can be applied equally well in real time, to historical records and to forecasts and hindcasts. The RMM index developed by WH04 is such an index. However, some limitations to the RMM index exist, as noted in the introduction. In particular, its use of OLR, a relatively noisy field with variability mostly limited to the Eastern Hemisphere, is one drawback that has been discussed in this paper. To this end, we have explored the potential benefits of a modified index of the MJO that uses VP200 rather than OLR to describe the convective/divergent component of the MJO but is otherwise similar.

The use of VP200 instead of OLR appears to better discriminate the MJO signal during boreal summer and may potentially capture precursors of the MJO before a strong local signal in convection is evident. The inverse Laplacian used to calculate VP200 acts as a smoother, which makes VP200 more sensitive to global-scale variations of convection/divergence rather than being concentrated on the Indo-Pacific warm pool like OLR. However, this increased sensitivity to convection in the Western Hemisphere comes at the expense of sensitivity in the Eastern Hemisphere, as well as during the boreal winter.

This enhanced sensitivity to identify the MJO during boreal summer through the use of VP200 is especially pertinent to detecting the MJO's modulation of Atlantic tropical cyclogenesis and hurricane activity. These variations in tropical cyclone activity were shown to be more coherent with the VPM PCs than with the original RMM indices. The implication of this result is that the variation of Atlantic tropical cyclones via the MJO is stronger and more robust than was implied by using the RMM indices. This difference increases the possibility of making useful intraseasonal predictions of Atlantic tropical cyclones. Since the VPM detects a higher number of MJO days during boreal summer when compared to RMM, there could also be stronger relationships with tropical cyclones in other basins.

Although the VPM indices have some benefits over the original RMM indices, there are also some drawbacks. The VPM indices are less sensitive to convection variations in the Eastern Hemisphere, as well as during boreal winter. The verification of this possibility awaits further study. More importantly, the VPM indices depend on analyses of VP200, which depends somewhat on the convective parameterizations in the assimilation model (e.g., Newman et al. 2000; Kinter et al. 2004). However, the new reanalyses such as provided by ERA-Interim appear to depict a more realistic intraseasonal

modulation of convection (Fu et al. 2011), so perhaps the quality of the analyzed VP200 is high enough to not be a deterrent for detection of the MJO.

Although we have emphasized a possible benefit of modifying one component of the MJO index as originally derived by WH04, this sort of MJO index, where by EOFs are calculated of equatorially averaged fields, is by no means the only approach worth pursuing. In fact, a general conclusion of this study is that there are alternative MJO indices that will have different sensitivities to the features of the MJO. These different indices may be more suitable for specific applications than is the RMM from WH04. To this end, we encourage and recommend exploration of alternative indices in order to promote a better understanding of the MJO and its global impacts.

Acknowledgments. The authors would like thank ECMWF and NCEP for providing the data in the study. We extend our gratitude to NASA for the Grants NNX09AD08G and NNX10AU44G, which supported this research. Interpolated OLR data were provided by the NOAA/OAR/ESRL PSD, Boulder, Colorado, from their website (<http://www.esrl.noaa.gov/psd/>). All figures were made using the NCAR Command Language (2013).

REFERENCES

- Annamalai, H., and K. R. Sperber, 2005: Regional heat sources and the active and break phases of boreal summer intraseasonal (30–50 day) variability. *J. Atmos. Sci.*, **62**, 2726–2748.
- Barrett, B. S., and L. M. Leslie, 2009: Links between tropical cyclone activity and the Madden–Julian oscillation phase in the North Atlantic and northeast Pacific basins. *Mon. Wea. Rev.*, **137**, 727–744.
- Belanger, J. I., J. A. Curry, and P. J. Webster, 2010: Predictability of North Atlantic tropical cyclone activity at intraseasonal time scales. *Mon. Wea. Rev.*, **138**, 4362–4374.
- Bergman, J. W., H. H. Hendon, and K. M. Weickmann, 2001: Intraseasonal air–sea interaction and the onset of ENSO. *J. Climate*, **14**, 1702–1719.
- Bessafi, M., and M. C. Wheeler, 2006: Modulation of south Indian Ocean tropical cyclones by the Madden–Julian oscillation and convectively coupled equatorial waves. *Mon. Wea. Rev.*, **134**, 638–656.
- Carvalho, L., C. Jones, and B. Liebmann, 2004: The South Atlantic convergence zone: Intensity, form, persistence, and relationships with intraseasonal to interannual activity and extreme rainfall. *J. Climate*, **17**, 88–108.
- Dee, D. P., and Coauthors, 2011: The ERA-Interim reanalysis: Configuration and performance of the data assimilation system. *Quart. J. Roy. Meteor. Soc.*, **137**, 553–597, doi:10.1002/qj.828.
- Frank, W. M., and P. E. Roundy, 2006: The role of tropical waves in tropical cyclogenesis. *Mon. Wea. Rev.*, **134**, 2397–2417.
- Fu, X., B. Wang, J.-Y. Lee, W. Wang, and L. Gao, 2011: Sensitivity of dynamical intraseasonal prediction skills to different initial conditions. *Mon. Wea. Rev.*, **139**, 2572–2592.
- Goswami, B. N., R. S. Ajaya Mohan, P. K. Xavier, and D. Sengupta, 2003: Clustering of low pressure systems during the Indian summer monsoon by intraseasonal oscillations. *Geophys. Res. Lett.*, **30**, 1431, doi:10.1029/2002GL016734.
- Gottschalck, J., and Coauthors, 2010: A framework for assessing operational Madden–Julian oscillation forecasts: A CLIVAR MJO working group project. *Bull. Amer. Meteor. Soc.*, **91**, 1247–1258.
- Goulet, L., and J.-P. Duvel, 2000: A new approach to detect and characterize intermittent atmospheric oscillations: Application to the intraseasonal oscillation. *J. Atmos. Sci.*, **57**, 2397–2416.
- Hall, J. D., A. J. Matthews, and D. J. Karoly, 2001: The modulation of tropical cyclone activity in the Australian region by the Madden–Julian oscillation. *Mon. Wea. Rev.*, **129**, 2970–2982.
- Haltiner, G. J., and R. T. Williams, 1980: *Numerical Prediction and Dynamic Meteorology*. John Wiley and Sons, 477 pp.
- Hendon, H. H., 1986: Streamfunction and velocity potential representation of equatorially trapped waves. *J. Atmos. Sci.*, **43**, 3038–3042.
- , and B. Liebmann, 1990: Composite study of onset of the Australian summer monsoon. *J. Atmos. Sci.*, **47**, 2227–2240.
- , and M. L. Salby, 1994: The life cycle of the Madden–Julian Oscillation. *J. Atmos. Sci.*, **51**, 2225–2237.
- Higgins, W., and W. Shi, 2001: Intercomparison of the principal modes of interannual and intraseasonal variability of the North American monsoon system. *J. Climate*, **14**, 403–417.
- Jones, C., and L. Carvalho, 2002: Active and break phases in the South American monsoon system. *J. Climate*, **15**, 905–914.
- Kalnay, E., and Coauthors, 1996: The NCEP/NCAR 40-Year Reanalysis Project. *Bull. Amer. Meteor. Soc.*, **77**, 437–471.
- Kim, J.-H., C.-H. Ho, H.-S. Kim, C.-H. Sui, and S. K. Park, 2008: Systematic variation of summertime tropical cyclone activity in the western North Pacific in relation to the Madden–Julian oscillation. *J. Climate*, **21**, 1171–1191.
- Kinter, J. L., M. J. Fennessy, V. Krishnamurthy, and L. Marx, 2004: An evaluation of the apparent interdecadal shift in the tropical divergent circulation in the NCEP–NCAR reanalysis. *J. Climate*, **17**, 349–361.
- Klotzbach, P. J., 2010: On the Madden–Julian oscillation–Atlantic hurricane relationship. *J. Climate*, **23**, 282–293.
- Lau, W. K. M., 2005: ENSO connections. *Intraseasonal Variability of the Atmosphere–Ocean Climate System*, W. K. M. Lau and D. E. Waliser, Eds., Springer, 277–308.
- Lavender, S., and A. Matthews, 2009: Response of the West African monsoon to the Madden–Julian oscillation. *J. Climate*, **22**, 4097–4116.
- Liebmann, B., and C. A. Smith, 1996: Description of a complete (interpolated) outgoing longwave radiation dataset. *Bull. Amer. Meteor. Soc.*, **77**, 1275–1277.
- , H. H. Hendon, and J. D. Glick, 1994: The relationship between tropical cyclones of the western Pacific and Indian Oceans and the phase of the MJO. *J. Meteor. Soc. Japan*, **72**, 401–412.
- Lin, H., G. Brunet, and J. Derome, 2008: Forecast skill of the Madden–Julian oscillation in two Canadian atmospheric models. *Mon. Wea. Rev.*, **136**, 4130–4149.
- Lorenc, A. C., 1984: The evolution of planetary-scale 200 mb divergent flow during the FGGE year. *Quart. J. Roy. Meteor. Soc.*, **110**, 427–441.

- Madden, R. A., and P. R. Julian, 1971: Detection of a 40–50-day oscillation in the zonal wind in the tropical Pacific. *J. Atmos. Sci.*, **28**, 702–708.
- , and —, 1972: Description of global-scale circulation cells in the Tropics with a 40–50 day period. *J. Atmos. Sci.*, **29**, 1109–1123.
- Maloney, E., and D. Hartmann, 2000a: Modulation of eastern North Pacific hurricanes by the Madden–Julian oscillation. *J. Climate*, **13**, 1451–1460.
- , and —, 2000b: Modulation of hurricane activity in the Gulf of Mexico by the Madden–Julian oscillation. *Science*, **287**, 2002–2004.
- , and J. Shaman, 2008: Intraseasonal variability of the West African monsoon and Atlantic ITCZ. *J. Climate*, **21**, 2898–2918.
- Matthews, A. J., 2004: Intraseasonal variability over tropical Africa during northern summer. *J. Climate*, **17**, 2427–2440.
- McPhaden, M. J., 1999: Genesis and evolution of the 1997–98 El Niño. *Science*, **283**, 950–954.
- Milliff, R. F., and R. A. Madden, 1996: The existence and vertical structure of fast, eastward-moving disturbances in the equatorial troposphere. *J. Atmos. Sci.*, **53**, 586–597.
- Mo, K. C., 2000: The association between intraseasonal oscillations and tropical storms in the Atlantic basin. *Mon. Wea. Rev.*, **128**, 4097–4107.
- Nakazawa, T., 1986: Intraseasonal variations of OLR in the tropics during the FGGE year. *J. Meteor. Soc. Japan*, **64**, 17–34.
- NCAR Command Language, 2013: NCL Version 6.0.0, UCAR/NCAR/CISL/VETS, doi:10.5065/D6WD3XH5.
- Newman, M., P. D. Sardeshmukh, and J. W. Bergman, 2000: An assessment of the NCEP, NASA, and ECMWF reanalyses over the tropical West Pacific warm pool. *Bull. Amer. Meteor. Soc.*, **81**, 41–48.
- North, G. R., T. L. Bell, R. F. Cahalan, and F. J. Moeng, 1982: Sampling errors in the estimation of empirical orthogonal functions. *Mon. Wea. Rev.*, **110**, 699–706.
- Roundy, P. E., C. J. Schreck III, and M. A. Janiga, 2009: Contributions of convectively coupled equatorial Rossby waves and Kelvin waves to the Real-Time Multivariate MJO Indices. *Mon. Wea. Rev.*, **137**, 469–478.
- Schreck, C. J., and J. Molinari, 2011: Tropical cyclogenesis associated with Kelvin waves and the Madden–Julian oscillation. *Mon. Wea. Rev.*, **139**, 2723–2734.
- Sobel, A. H., and D. Kim, 2012: The MJO-Kelvin wave transition. *Geophys. Res. Lett.*, **39**, L20808, doi:10.1029/2012GL053380.
- Sperber, K. R., J. M. Slingo, and H. Annamalai, 2000: Predictability and the relationship between subseasonal and interannual variability during the Asian summer monsoon. *Quart. J. Roy. Meteor. Soc.*, **126**, 2545–2574.
- Straub, K., 2013: MJO initiation in the Realtime Multivariate MJO Index. *J. Climate*, **26**, 1130–1151.
- Takayabu, Y. N., T. Iguchi, M. Kachi, A. Shibata, and H. Kanzawa, 1999: Abrupt termination of the 1997–98 El Niño in response to a Madden–Julian oscillation. *Nature*, **402**, 279–282.
- Ventrice, M. J., C. D. Thorncroft, and P. E. Roundy, 2011: The Madden–Julian Oscillation’s influence on African easterly waves and downstream tropical cyclogenesis. *Mon. Wea. Rev.*, **139**, 2704–2722.
- Waliser, D. E., 2006: Intraseasonal variations. *The Asian Monsoon*, B. Wang, Ed., Springer, 787 pp.
- Wheeler, M. C., and H. H. Hendon, 2004: An all-season real-time multivariate MJO index: Development of an index for monitoring and prediction. *Mon. Wea. Rev.*, **132**, 1917–1932.
- , and J. L. McBride, 2005: Australian–Indonesian monsoon. *Intraseasonal Variability in the Atmosphere–Ocean Climate System*, W. K. M. Lau and D. E. Waliser, Eds., Springer, 125–173.
- Xue, Y., W. Higgins, and V. Kousky, 2002: Influences of the Madden Julian Oscillation on temperature and precipitation in North America during ENSO-neutral and weak ENSO winters. Preprints, *Workshop on Prospects for Improved Forecasts of Weather and Short-term Climate Variability on Subseasonal Time Scales*, NASA Goddard Space Flight Center, 4 pp. [Available online at http://www.cpc.ncep.noaa.gov/products/precip/CWlink/daily_mjo_index/CPCmjoindex.pdf.]
- Zhang, C., 2005: Madden–Julian oscillation. *Rev. Geophys.*, **43**, 1–36.
- , and J. Gottschalck, 2002: SST anomalies of ENSO and the Madden–Julian oscillation in the equatorial Pacific. *J. Climate*, **15**, 2429–2445.